J Nanopart Res (2015)17:294
DOI 10.1007/s11051-015-3073-7

RESEARCH PAPER

Synthesis and characterization of $CoFe_2O_4$ magnetic nanotubes, nanorods and nanowires. Formation of magnetic structured elastomers by magnetic field-induced alignment of $CoFe_2O_4$ nanorods

P. Soledad Antonel · Cristiano L. P. Oliveira · Guillermo A. Jorge · Oscar E. Perez · A. Gabriela Leyva · R. Martín Negri

Received: 9 March 2015 / Accepted: 9 June 2015

Abstract Magnetic $CoFe_2O_4$ nanotubes, nanorods and nanowires were synthesized by the template method. The materials are highly crystalline and formed by compactly packed ceramic particles whose equivalent size diameter depends on the nanostructure type. Nanotubes and nanorods present the remarkable characteristic of having very large coercive fields (1000–1100 Oe) in comparison with nanoparticles of the same crystallite size (400 Oe) while keeping similar saturation magnetization (53–55 emu/g). Nanorods were used as filler material in polydimethylsiloxane elastomer composites, which were structured by curing in the presence of uniform magnetic field, H_{curing}. In that way the nanorods agglomerate in the cured elastomer, forming needles-like structures (pseudo-chains) oriented in the direction of H_{curing}. SEM analysis show that pseudo-chains are formed by bunches of nanorods oriented in that direction. At the considered filler concentration (1 % w/w), the structured elastomers conserve the magnetic properties of the fillers, that is, high coercive fields without observing magnetic anisotropy. The elastomer composites present strong elastic anisotropy, with compression constants about ten times larger in the direction parallel to the pseudo-chains than in the perpendicular direction, as determined by compression stress–strain curves. That anisotropic factor is about three-four times higher than that observed when using spherical $CoFe_2O_4$ nanoparticles or elongated

Guillermo A. Jorge: on leave from Laboratorio de Bajas Temperaturas, UBA. Argentina.

P. S. Antonel · R. M. Negri (✉)
Departamento de Química Inorgánica, Analítica y Química Física, Facultad de Ciencias Exactas y Naturales, Instituto de Química Física de Materiales, Ambiente y Energía (INQUIMAE), Universidad de Buenos Aires, Ciudad Universitaria, Pabellón 2, C1428EGA Ciudad Autónoma de Buenos Aires, Argentina
e-mail: rmn@qi.fcen.uba.ar

C. L. P. Oliveira
Grupo de Fluidos Complexos, Instituto de Física, Universidade de São Paulo, São Paulo, Brazil

G. A. Jorge
Instituto de Ciencias, Universidad Nacional de General Sarmiento, Buenos Aires, Argentina

O. E. Perez
Departamento de Industrias, Facultad de Ciencias Exactas y Naturales, Universidad de Buenos Aires, Buenos Aires, Argentina

A. G. Leyva (✉)
Grupo de Materia Condensada, Centro Atómico Constituyentes, Comisión Nacional de Energía Atómica (Argentina) and Escuela de Ciencia y Tecnología, Universidad Nacional de San Martín, Av. Gral. Paz y Constituyentes, 1499, San Martín, Pcia. de Buenos Aires, Argentina
e-mail: leyva@tandar.cnea.gov.ar

Published online: 08 July 2015

Ni nanochains. Hence, the use of morphological anisotropic structures (nanorods) results in composites with enhanced elastic anisotropy. It is also remarkable that the large elastic anisotropy was obtained at lower filler concentration compared with the above-mentioned systems (1 % w/w vs. 5–10 % w/w).

Keywords Magnetic nanorods · Magnetic nanotubes · Structured elastomers · Magnetic composites

Introduction

The preparation of magnetic nanomaterials such as nanotubes, nanorods, and nanowires attracts considerable attention due to the possibility of tuning the magnetic properties by changing the morphology of the material at the nanoscale (Bance et al. 2014; Bechelany et al. 2012; Cernea et al. 2014; Escrig et al. 2008; Forster et al. 2003; Hussain et al. 2011; Jung et al. 2005; Ko et al. 2012; Kohli et al. 2010; Pereira et al. 2013; Tsai et al. 2008). Additionally, magnetic nanomaterials can be used as fillers in elastomer polymers composites. Several magnetic nanoparticles have been used to obtain magnetic elastomers, consisting of an elastic matrix embedded with magnetic materials (the fillers) that confers the properties of interest to the final composite (Bica et al. 2012; Chen and Jerrams 2011; Danas et al. 2012; Høyer et al. 2012; Lorenzo et al. 2012; Macias et al. 2012; Mordina et al. 2014; Semeriyanov et al. 2013; Shahrivar and de Vicente 2013). Additionally, it is possible to align the fillers applying external magnetic fields during preparation. The alignment of magnetic nanoparticles by applying a uniform magnetic field during the thermal curing of the polydimethylsiloxane (PDMS) or during solvent evaporation in the case of styrene-butadiene rubber (SBR) matrices has been described in previous works of our group (Antonel et al. 2011; Antonel et al. 2012; Butera et al. 2012; Landa et al. 2013; Mietta et al. 2012; Mietta et al. 2013, Mietta et al. 2014; Ruiz et al. 2012; Ruiz et al. 2015). Those elastic composites are referred as *structured*, where the filler nanomaterials join together and form needle-like structures (pseudo-chains) inside the polymer matrix, which are aligned in the direction of the magnetic field applied during preparation. The potentiality of these materials for developing sensors is illustrated in Mietta et al. (2013) and Ruiz et al. (2015) where superparamagnetic nanomagnetites covered with metallic silver were used as fillers, obtaining -after preparation in the presence of magnetic fields- structured elastomer composites which are simultaneously magnetic and electrical conductors, presenting magnetoresistivity and piezoresistivity in a single matrix with anisotropic behavior. The degree of anisotropy in the physical properties of the structured composite is dependent on the concentration of fillers and its morphology (e.g., nanoparticles, nanobars, etc.). For instance, some recent results obtained in our group (Landa et al. 2013) show that magnetic and elastic anisotropy can be induced with very low amount of fillers if nickel nanochains are used as fillers instead of nickel nanoparticles. Despite of the relatively generalized use of nano or micro particles, magnetic nanotubes, nanorods, or nanowires have been no explored as fillers in structured magnetic elastomers. Hence, the aims of the present work are to describe the synthesis and characterization of cobalt-ferrite ($CoFe_2O_4$) nanotubes, nanorods, and nanowires and then to explore the possibility of inducing elastic and magnetic anisotropy in an elastomer composite by using magnetic nanorods as fillers in concentration lowers than the used in previous works for the case of $CoFe_2O_4$ nanoparticles (e.g., lower than 5% w/w). The application of $CoFe_2O_4$ nanorods was investigated by incorporating this material into PDMS, and the filler-polymer composite was thermally cured in the presence of a uniform magnetic field. It is important to remark the final composite is not a ferrofluid (or a magnetorheological fluid) nor a fluid gel but an elastic non-fluid material which can be processed for its applications as the active material in a device.

Materials and methods

Synthesis of $CoFe_2O_4$ nanotubes, nanorods, and nanotubes

$CoFe_2O_4$ nanostructures were obtained using the template method, as already reported in several articles by one of the present authors (Bellino et al. 2007; Fuentes et al. 2008a; Fuentes et al. 2008b; Leyva et al. 2004, Leyva et al. 2006; Levy et al. 2003) but

using $Fe(NO_3)_3$ $9H_2O$ and $Co(NO_3)_2$ $6H_2O$ as precursors. Each nitrate (in a molar ratio Co:Fe 1:2) was dissolved in pure water to obtain a 1 M cations solution (20 mL). To favor the dissolution, three drops of concentrated nitric acid were also added. Porous polycarbonate films were used as polymeric templates (Isopore membrane films, Millipore; pore pass diameters = 100 and 800 nm). The films were embedded with the precursor solution using a previously reported *ad hoc* syringe filtration system which ensures that the total volume of the pores is filled (precursors are confined in the pores). Then, the next step was the dehydration and denitrification of the confined precursors in a commercial microwave oven, applying an output power of 800 W for 3 min. Finally, to obtain the desired nanostructures, the templates were burnt off in a standard furnace employing a thermal treatment (calcination) up to 800 °C (for 800 nm filters) and up to 600, 700, or 800 °C (for 100 nm filters). The final temperature was maintained during 10 min, and then the furnace was allowed to cool freely toward room temperature.

Summarizing, the nanostructures are obtained filling porous polycarbonate template with the stoichiometric nitric solutions of cations using a syringe filtration device, followed by the denitration process of the confined precursor in a microwave oven. By adjusting the time and energy applied to the sample, it is possible to accomplish this reaction without producing damage to the polycarbonate film. Then the template is sacrificed during the next thermal treatment in a standard furnace at the final temperature of calcination. The synthesis is highly reproducible, that is, nanomaterials with quantitatively similar morphology and crystallinity were obtained in different synthesis. Sixty filters were used in each synthesis to obtain the amount of material required for characterization studies.

Different nanostructures can be obtained according to the size of the pores, precursor concentration, and the final temperature of calcination. For instance, hollowed structures (nanotubes) were obtained when using 800 nm filters, and while filled structures when using 100 nm filters. In the last case, when the final temperature during the calcination process was 600 or 700 °C, we obtained nanorods, but if this temperature was set at 800 °C, then the structures formed were nanowires. In Table 1, a summary of the reaction conditions is presented:

Preparation of PDMS–$CoFe_2O_4$ (nanorods) structured elastomer composites

The details for the preparation of structured composites of PDMS-magnetic fillers have been described in previous works (Antonel et al. 2011; Antonel et al. 2012; Butera et al. 2012; Landa et al. 2013; Mietta et al. 2012; Mietta et al. 2013, Mietta et al. 2014; Ruiz et al. 2012). PDMS base and cross-linker agent (Sylgar 184, Dow Corning) were mixed in proportions of 10:1 (w/w) at room temperature and then loaded with the magnetic nanorods F100-700. The amounts of PDMS and fillers (1 % w/w of nanorods F100-700 in the final material) were weighted during mixing on an analytical balance, homogenized, and placed at room temperature in a vacuum oven for about two hours until the complete absence of any air bubble. The still fluid samples were incorporated into a specially designed cylindrical mold (1 cm diameter × 1 cm length) and placed in between the magnetic poles of a Varian Low Impedance Electromagnet (model V3703) which provides highly homogeneous steady magnetic fields. The mold was rotated at 30 rpm and heated at (75 ± 5) °C in the presence of a uniform magnetic field, referred as H_{curing}, during 4 h to obtain a cured material ($\mu_0 H_{curing} = 0.3$ T). Controls without applying the magnetic field were also performed.

Instrumentation

X-ray powder diffraction analysis (XRD) was performed with a Philips X-Pert diffractometer using CuK_α radiation ($\lambda = 0.154056$ nm), and the average size of the crystallites was determined by the Debye–Scherrer equation. The morphology of the nanotubes, nanorods, and nanowires and its composites were studied using a scanning electron microscope (SEM) fitted with a field-emission source (FESEM Zeiss Supra 40 Gemini) coupled to a energy dispersive spectroscopy (EDS) detector (Oxford Instruments, model INCAx-Sight; detection limit: 0.1 % w/w). A Philips EM 301 Transmission Electron Microscope, TEM was also used.

Small angle x-ray scattering (SAXS) experiments were performed in a laboratory-based equipment, NANOSTAR™ from Bruker at the Laboratory of Crystallography, Institute of Physics, University of São Paulo, Brazil. The powder samples (not diluted) were exposed to the X-rays using a Scotch Tape™ to support the samples, and background signal was taken using the scattering from the tape alone (exposition

Table 1 Synthesis conditions for $CoFe_2O_4$ nanomaterials

Morphology	Filter's pore size (nm)	Temperature of calcination, (after microwave heating) (°C)	Sample code
Nanotubes	800	800	F800-800
Nanorods	100	700	F100-700[a]
		600	F100-600
Nanowires	100	800	F100-800

[a] Used as filler in PDMS-structured composites

time: 900 s). Data treatment was performed using the package SUPERSAXS (developed by Oliveira and Pedersen, unpublished). The experimental data are displayed as Intensity, $I(q)$, versus the momentum transfer q, $q = (4\ \pi/\lambda)\sin\theta$, where λ is the radiation wavelength and 2θ is the scattering angle. The measured q interval was 0.085–3.4 nm^{-1}. A model based on a polydispersed (Schulz–Zimm size distribution) system of hard spheres (PHS) combined with the formation of fractal aggregates and hard-sphere interaction was used to describe the experimental data. A detailed description of the model is presented in the Appendix. Fitting of experimental data by these models allows obtaining the average sphere radius R_{av}, the polydispersivity σ_R, the fractal domain size ξ, the fractal dimension D, the effective hard-sphere radius $\langle R_{HS}\rangle$, and the effective volume fraction η.

A LakeShore 7400 vibrating sample magnetometer (VSM) was used for recording magnetization curves at room temperature. The samples were prepared by packing with Teflon tape slices of 10–20 mg of each composite.

The analysis of elasticity and the Youngs modulus determination were performed using a Stable Microsystems TA-XT2i Texture Analyzer which compresses the sample at a constant speed (100 μm/s) in the range of strains between 8 to 25% of the initial thickness (Negri et al. 2010). The thickness in absence of compression, referred as L_i, was fixed to 3 mm in all cases.

Results and discussion

Characterization of $CoFe_2O_4$ nanotubes and nanowires

Figure 1 are SEM images of the $CoFe_2O_4$ nanotubes. Figure 2 shows SEM images of $CoFe_2O_4$ nanorods. Figures 3 and 4 show TEM and SEM images of nanowires, respectively. A representative selected-area electron diffraction (SAED) pattern of nanorods is shown in Fig. 4. Table 2 shows the systematic increase of the aspect ratio when going from particles, tubes, rods, and wires, in this order.

SEM and TEM images show that the synthesized nanostructures seem to be actually constituted by particles of inorganic material, spatially arranged to form the tubes, rods, and wires. For instance, in the case of nanorods F100-700 (Fig. 2), the ceramic grains appear with average size about 60 nm (observed by SEM) although presenting high dispersion. XRD and SAXS experiments were performed in order to further investigate these structures. X-ray powder diffraction patterns (XRD indicates that the synthesized $CoFe_2O_4$ nanotubes and nanorods are crystalline single phases (Fig. 5).

The XRD peaks correspond to the cubic inverse spinel type lattice, as expected for $CoFe_2O_4$ (ICDD 03-0864) and coincident with the one reported for $CoFe_2O_4$ nanoparticles in our previous article (Antonel et al. 2011). The crystallite size obtained using the Debye–Scherrer equation (see $2R_c$ in Table 3) is clearly larger for nanotubes than for nanorods. For instance, the crystallite size for nanorods F1-700 is about 20 nm while for nanotubes is four times larger (82 nm). The 20 nm crystallite size recovered for F1-700 nanorods is coincident with the value obtained for the synthesized nanoparticles that were used as fillers in elastomer matrixes in the previous work. For this reason, nanorods F1-700 were chosen to prepare the magnetic elastomers, in order to compare the results with those obtained using $CoFe_2O_4$ nanoparticles. Finally, it can be observed that in nanorods, the crystallite size increases with the final temperature of calcination (Table 3).

SAXS data (Fig. 6) were fitted by the Fractal Cluster Model, which assumes that at a nanometric

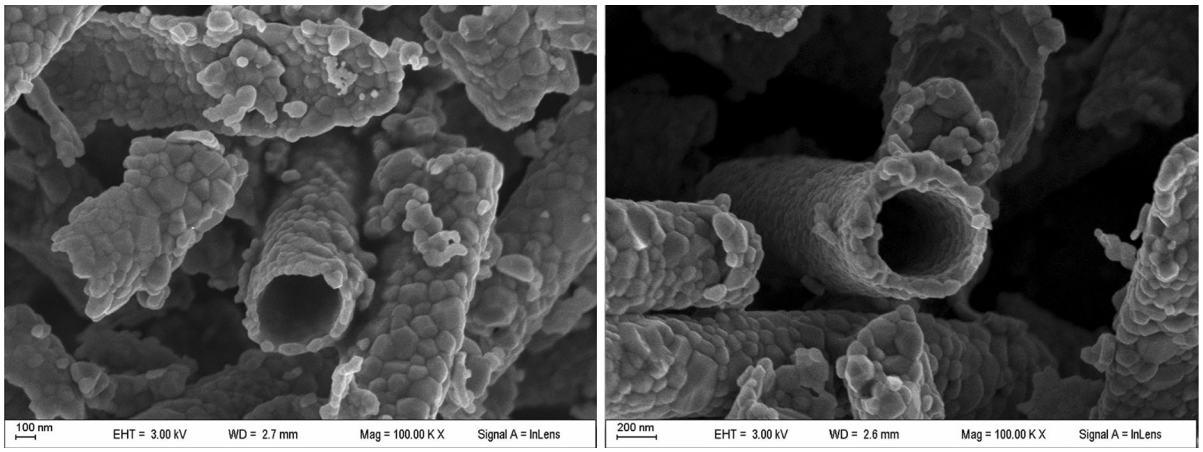

Fig. 1 SEM images of $CoFe_2O_4$ nanotubes (sample code: F800-800, Table 1)

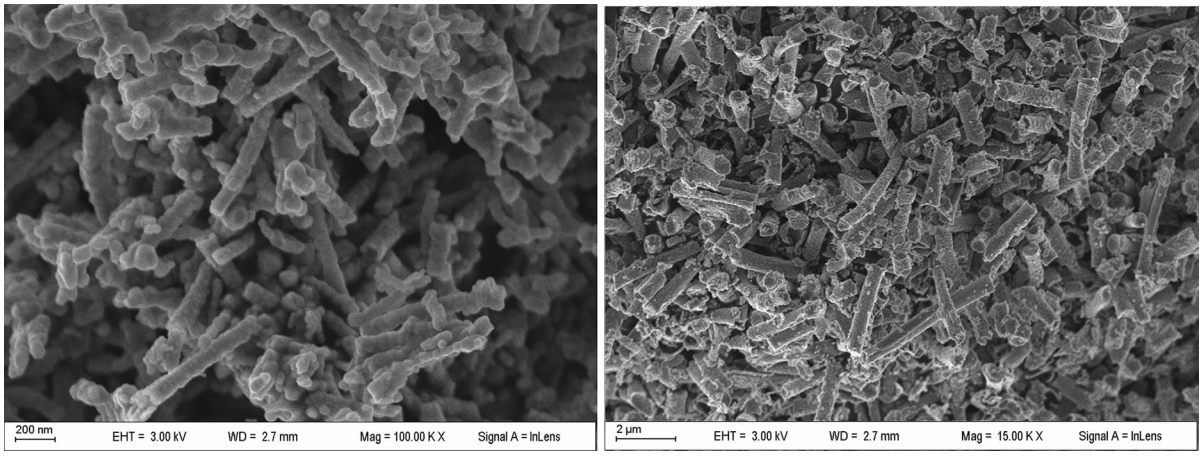

Fig. 2 SEM images of $CoFe_2O_4$ nanorods (sample code: F100-700, Table 1)

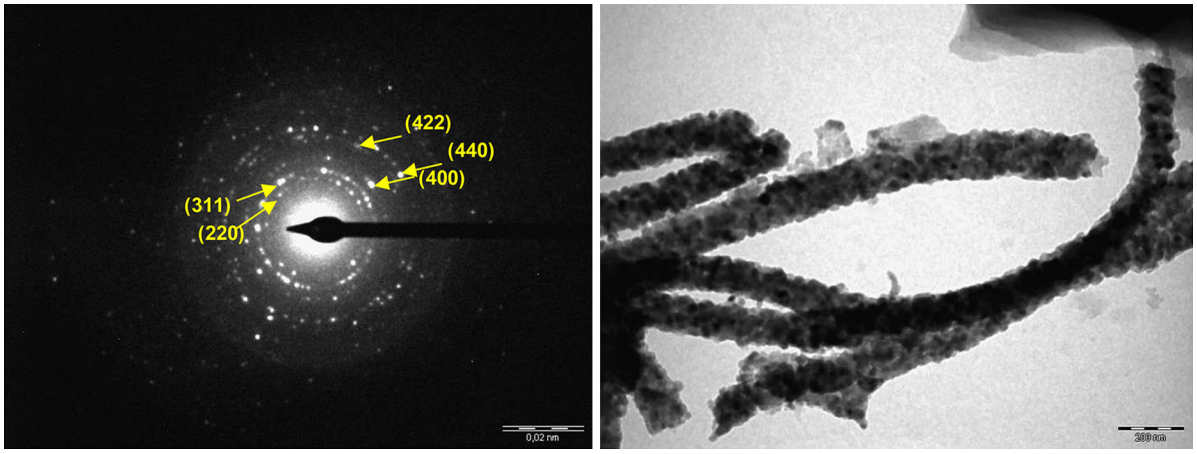

Fig. 3 SAED and TEM images of $CoFe_2O_4$ nanorods (sample code: F100-700, Table 1). SAED indexes according to Gajbhiye et al. 2010

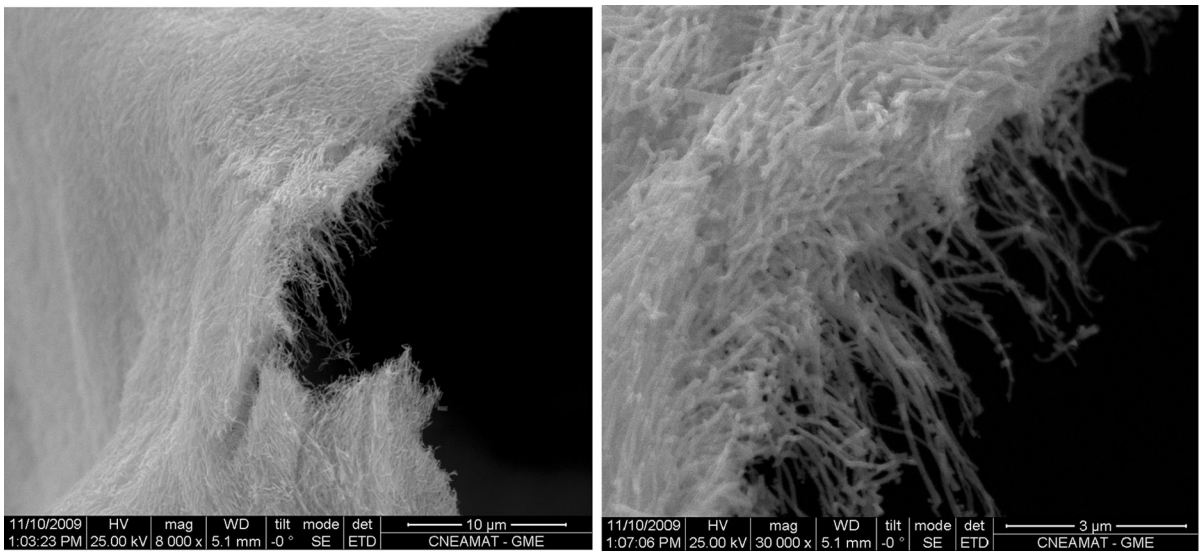

Fig. 4 SEM images of $CoFe_2O_4$ nanowires (sample code: F100-800, Table 1)

Table 2 Morphological parameters obtained from SEM images

Material $CoFe_2O_4$	Average diameter, d (SEM) (nm)	Average length, l (SEM) (nm)	Aspect ratio (SEM) (l/d)
Nanoparticles-A[a]	12	–	1
Nanotubes F800-800	700	4000	6
Nanorods F100-700	142	1285	9
Nanowires F100-800	58	3529	56

[a] From Antonel et al. (2011) where value of d is the maximum of size distribution calculated from TEM images

scale, there are clusters formed by the so-called subunits, being those clusters the responsible of X-ray dispersion. The subunits are modeled as polydispersed spheres, namely $\langle 2R \rangle$ and $2\sigma_R$ to the average size and standard deviation for the size distribution of the subunits, respectively. The clusters are assumed to have a fractal dimension, D, forming ramified structures with a correlation distance, ξ Depending on the size of the fractal clusters, it might appear interactions among the clusters, which can be characterized by an overall hard-sphere radius, $\langle R_{HS} \rangle$ and an effective volume fraction η (note that $\langle 2R_{HS} \rangle$ must be much larger than $\langle 2R \rangle$). All these features are accounted by the Fractal Cluster Model presented in the Appendix.

In all cases (nanoparticles, tubes, and rods), excellent fits of SAXS data were obtained with the Fractal Cluster Model. This fractal behavior of the $CoFe_2O_4$ nanomaterials is very different to that previously reported by us in the case of nickel (Ni) nanoparticles of similar sizes, since for that Ni nanoparticles, no fractal clusters were formed (Landa et al. 2013). Table 3 shows that the materials are described as 3-dimensional fractals (D close to 3) formed by subunits (size of subunits lower than 1 nm, distribution given by $\langle 2R \rangle$ and $2\sigma_R$, Table 3). These subunits form clusters whose overall size is characterized by 2ξ and/or $\langle 2R_{HS} \rangle$, whose recovered values have similar order of magnitude, about 20-50 nm depending of the material (and also in the same order than the crystallite size obtained from Debye–Scherrer and SEM pictures). The fact that SAXS data can be modeled by the Fractal Cluster Model in the case of the nanotubes and nanorods is in agreement with the structures observed by SEM, which also showed that the synthesized materials are formed by ceramic grains of inorganic material with a relatively large size polydispersion.

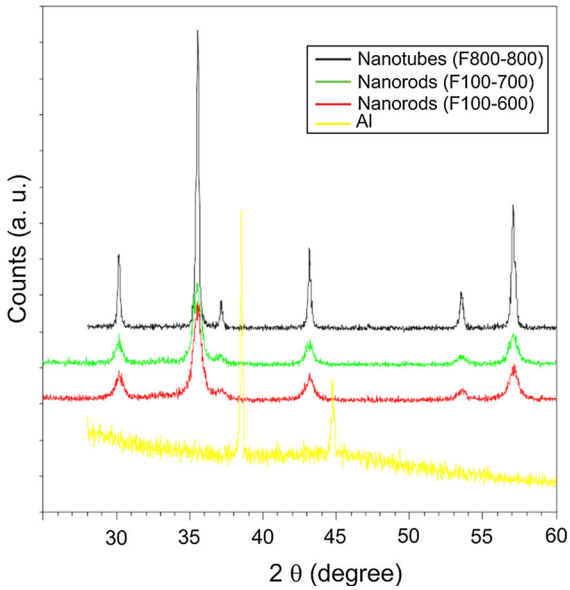

Fig. 5 XRD of $CoFe_2O_4$ nanomaterials. XRD of the substrate (Al) is shown for comparison

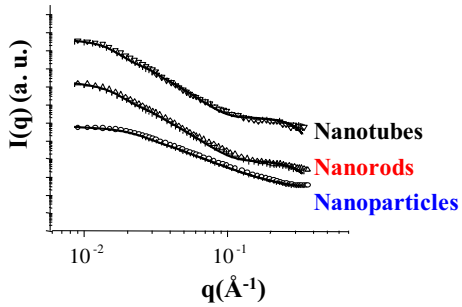

Fig. 6 SAXS results for nanoparticles-A, nanotubes (F800-800), and nanorods (F100-700). The *solid lines* represent fits by the Fractal Cluster Model

The size of the subunits recovered from SAXS is roughly about 6-10 Å (see $\langle 2R \rangle$ and $2\sigma_R$ in Table 3), which is in the order of lattice parameter $CoFe_2O_4$, 8.392 Å (Thang et al. 2007). Since for nanorods, the crystallite size $2R_c$ is about 18 nm (Table 3), then the number of subunits within a crystallite is about 6×10^3 ($\cong (2R_c/\langle 2R \rangle)^3$). One can assume this relation due to the fact that the fractal dimension D is close to 3, indicating a volume fractal, that is, about 6×10^3 unit cells group forming a crystallite. In turn, the crystallites are grouped to form branched structures, the fractal clusters, which are assumed as rigid spheres presenting average size about 39 nm for nanorods ($\langle 2R_{HS} \rangle$ in Table 3). That value of $\langle 2R_{HS} \rangle$, recovered from SAXS, is in good agreement with the average size observed in the SEM images for the agglomerates that forms the nanorods ($\cong$60 nm) considering the high dispersion, experimental errors from different techniques and model assumptions. Within this frame, each fractal is formed by an average of $(\langle 2R_{HS} \rangle / 2R_c)^3 = (39/18)^3 \cong 10$ crystallites.

Magnetic properties of $CoFe_2O_4$ nanowires and nanotubes

The magnetization curves at room temperature (25 °C) for $CoFe_2O_4$ nanotubes and nanorods are shown in Fig. 7, observing magnetic hysteresis loops that indicate the ferromagnetic behavior of both nanostructures at room temperature.

The magnetization curves of both nanostructures are almost coincident at room temperature, indicating that their magnetic parameters (remanence magnetization, M_r, saturation magnetization, M_s, and coercive field, H_c) are practically identical for nanorods and nanotubes. The comparison of magnetic parameters between nanoparticles, nanotubes, and nanorods is presented in Table 4. When comparing $CoFe_2O_4$

Table 3 Parameters recovered from SAXS analysis fitted by the Fractal Cluster Model

Material $CoFe_2O_4$	Fractal dimension (D)	‹2R› (Å)	$2\sigma_R$ (Å)	2ξ (nm)	‹2R›$_{HS}$ (nm)	Crystallite size[a] ($2R_c$, nm)
Nanoparticles-A	2.74 ± 0.01	≈6	≈4	12.8 ± 0.2	26.2 ± 0.2	20 ± 3[b]
Nanotubes F800-800	3.09 ± 0.01	≈6	≈4	29 ± 1	42 ± 1	82 ± 3
Nanorods F100-700	3.09 ± 0.01	≈6	≈4	25 ± 1	39 ± 1	18 ± 2[c]

[a] From XRD-Debye–Scherrer

[b] From Antonel et al. (2011)

[c] For the case of F100–600 nanorods the recovered average crystallite size is slightly smaller, (14 ± 1) nm

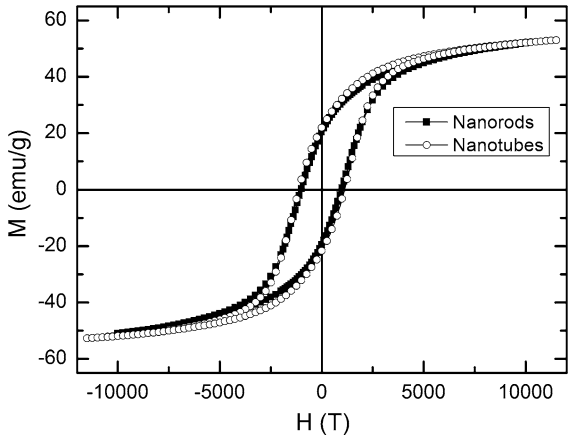

Fig. 7 Magnetization curves at 25 °C for nanotubes (F800-800) and nanorods (F100-700)

nanotubes–nanorods versus $CoFe_2O_4$ nanoparticles-A, it can be remarked the huge increase of the coercive field, *H*c, of the nanotubes–nanorods in comparison with nanoparticles by a factor of three, approximately, irrespectively of the crystallite size. Although the increase of H_c in nanowires has been reported (see, for example, Grobert et al. 1999; Jung et al. 2005), the huge increase of H_c is a remarkable characteristic of the nanotubes–rods described here. For instance, when comparing between Ni nanoparticles (single domain, $2R_c \cong 13$ nm) and Ni nanochains (aspect ratio = 8) described in one of our previous works, it was observed that H_c is 20 % *larger for nanoparticles*. But in the present case of $CoFe_2O_4$, H_c is 150 % *larger for nanorods* (aspect ratio = 9) than nanoparticles-A (single domains, $2R_c \cong 20$ nm) (similar changes observed for nanotubes).

This huge increase of H_c suggests that the main process dominating the reversal magnetization is of different nature in the tubes–rods than in nanoparticles. The $CoFe_2O_4$ nanoparticles considered here (referred as nanoparticles-A, 20 nm) are in the single-ferromagnetic domain regime (Antonel et al. 2011) for which the coherent rotation of the spins is expected to be the main mechanism of magnetization reversal. On the other hand, the nanotubes and nanorods presented in this work are formed by ceramic grains of about 60 nm size that join appropriately trough grain boundaries, forming the nanostructures. The interactions between spins in these structures are not easy to be accounted by simple models. According to Leslie-Pelecky and Rieke (1996) in systems with a large number of grain boundaries and interfaces, interactions must be considered, that is, the magnetic behavior cannot be predicted by simple models which did not include strong interactions between many magnetic grains. In those cases, magnetic properties are dominated by exchange energies, magnetostatic, and energy associated to grain boundary effects, while anisotropic effects (included in the anisotropic constant, *K*) may have secondary relevance. Moreover, domain walls in those systems must take in to account the grain boundaries as defects in which rotational symmetry is violated (disclinations), and the magnetization changes occur not via the motion of domain walls but instead via disclination motions, as those described in the Holz–Scherer model (Holz and Scherer 1994). In particular, coercive fields, H_c, can be dominated by disclination motions, whose contribution to the energetic (according to the above model) must be present in our nanorods and nanotubes but not in the nanoparticles-A. In systems like nanoparticles, or even nanotubes of smaller sizes than the ones presented here, other reversal mechanisms are currently proposed, such as the propagation of a domain wall, vortex wall, etc. (Albrecht et al. 2011; Bance et al. 2014; Chen et al. 2010; Forster et al, 2003; Landeros and Núñez 2010; Usov and Serebryakova 2014). For instance, Escrig et al. (2008) showed that for Ni nanotubes of diameters below 60 nm, the nucleation and propagation of domain walls are the dominant reversal mechanism. However, those mechanisms hardly apply in larger structures like those described here. In the present nanorods and nanotubes, the presence of disclinations between grain boundaries in the nanotubes–rods is a factor that contributes to enhance H_c and can probably explain the larger values of H_c in our nanotubes–rods than in nanoparticles-A of similar crystallinity. Disclinations are strongly dependent on the morphology of ceramic grains arrays in the nanostructure, and its dependence on these factors is beyond the present work.

Table 4 Magnetic properties

Material ($CoFe_2O_4$)	Ms (emu/g)	Mr (emu/g)	Hc (Oe)
Nanoparticles-A[a]	65	12	400
Nanotubes	55	22	1100
Nanorods	53	21	1000

[a] From Antonel et al. (2011)

Since M_s does not change drastically (as H_c does) for nanoparticles-A and nanotubes/rods, then the remanence magnetization, M_r, increases by a factor of two in tubes–rods as expected in systems with similar M_s but larger H_c values (Table 4).

Structured magnetic elastomers of PDMS–$CoFe_2O_4$ nanorods

In previous works, we used $CoFe_2O_4$ nanoparticles (referred as nanoparticles-A) and Ni nanochains as fillers in PDMS-structured composites. Now, by setting the synthesis conditions, we obtained magnetic nanorods which present similar crystallite size ($2R_c$) and M_s than the $CoFe_2O_4$ nanoparticles-A and also similar aspect ratio than Ni nanochains. Its major difference is the large H_c of the $CoFe_2O_4$ nanorods, about three times larger than the nanoparticles-A, as described in the previous section. Then, these $CoFe_2O_4$ nanorods were chosen as fillers in the same type of structured elastomer composites, in order to explore the effect of its presence on the magnetic and elastic properties of the organic matrix, comparing with those induced when using $CoFe_2O_4$ nanoparticles-A and Ni nanochains. The obtained results are presented in this section.

$CoFe_2O_4$ nanorods (1 % w/w) are dispersed in the PDMS matrix at room temperature, when the system is still fluid and then thermally cured in the presence of a uniform magnetic field (H_{curing}) as described in "Materials and methods" section. The experimental conditions match exactly the same than in the previous cases of $CoFe_2O_4$ nanoparticles-A and Ni nanochains (Antonel et al. 2011; Landa et al. 2013) in order to allow a proper comparison. After curing, an elastic composite is obtained with formation of needles (pseudo-chains), aligned in the direction of the magnetic field applied when curing. Millimeter slices of these composites can be cut for using in different tests. Pseudo-chains are not formed in the absence of H_{curing}.

The amount of $CoFe_2O_4$ nanorods required for observing pseudo-chains (1 % w/w) is much lower than that required in the case of $CoFe_2O_4$ nanoparticles-A (5 % w/w), which is a very promising result from a practical point of view, since synthesis of nanorods—comparing with nanoparticles—is much time costing. The 1 % w/w proportion is even lower than that required for Ni nanochains (2 % w/w) under the same experimental conditions of preparation.

All fillers were observed grouped in the pseudo-chains (no isolated fillers were detected by SEM). A SEM image of one cut of the slices is presented in Fig. 8, where the inside of one pseudo-chain is captured. As observed, the pseudo-chain is formed by bunches of nanorods. The dimensions and aspect ratio of the nanorods in the pseudo-chains appear very similar to that presented in Table 2. That is, nanomaterials agglomerate during curing to form the pseudo-chains, without observing *"fusion"* of nanorods. The individual nanorods can be clearly observed, also aligned preferentially in the direction of H_{curing}.

Magnetization curves of the composites were measured in the directions parallel (//) and perpendicular ($\perp$) to the pseudo-chains (Fig. 9). The angle formed between the direction of the sensing field in the measurement, and H_{curing} is referred as α ($\alpha = 0°$ and $\alpha = 90°$ for the directions // and $\perp$, respectively). As expected considering the low amount of magnetic material in the composite, the magnetization signals are about 99 % lower in the composites than those of the powder, a factor which is in very good agreement with the proportion of inorganic material in the composite. Hence, the curves shown in Fig. 9 are normalized to the respective observed M_s value, which are similar for composites with 1 % w/w nanorods and nanoparticles-A. The values of H_c in the composites are similar to the values in the powders which mean that the nanorods conserve their magnetic properties in the composites.

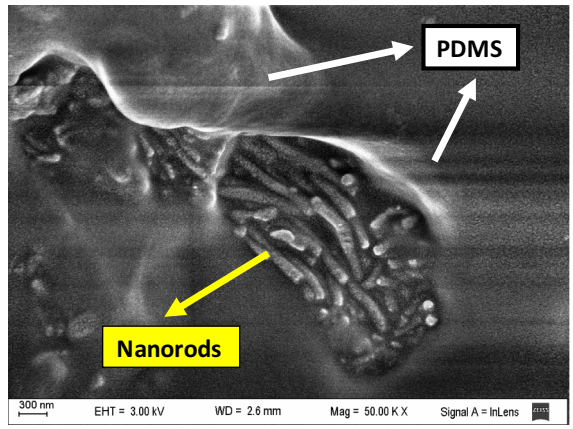

Fig. 8 SEM image of a cut slice of PDMS–$CoFe_2O_4$ nanorod-structured composite. The image captures one pseudo-chain formed by bunches of F100-700 nanorods

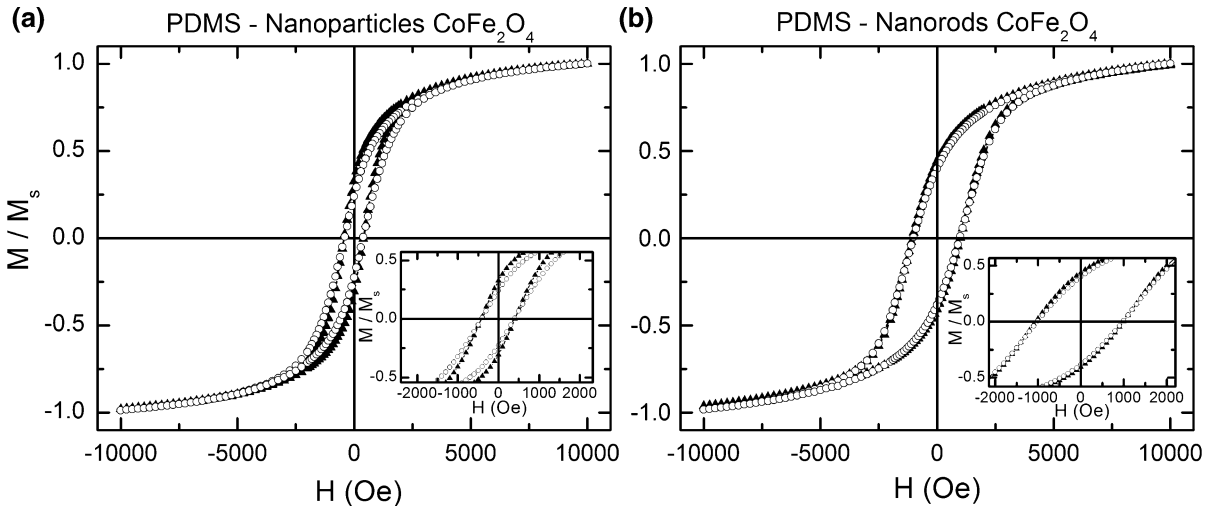

Fig. 9 Normalized magnetization curves (25 °C) in PDMS–$CoFe_2O_4$-structured composites using **a** nanoparticles (5 % w/w) and **b** nanorods (1 % w/w). The difference between curves // (-▲-) and ⊥ (-○-) to the pseudo-chains cannot be appreciated. *Inset* zoom of each normalized magnetization curve at low magnetic fields

Although the absolute values obtained from the magnetization curves in such diluted systems must be considered with caution, the main feature remains: H_c when using nanorods as fillers are much larger than for nanoparticles-A (see Fig. 9), with similar M_s and the consequent larger M_r for the case of nanorods as fillers. The remarkable difference of H_c values between nanorods and nanoparticles in the composites can be clearly observed by comparing the left (nanoparticles) and right (nanorods) plots in Fig. 9. Hence, in spite of the fillers grouped forming pseudo-chains in the composites, its individual characteristic is conserved, in agreement with the SEM observation (Fig. 8) describing the pseudo-chains as bunched of the original fillers (similar results were obtained in the previous work for nanoparticles-A).

No significant differences of the magnetization curves recorded in directions // (-▲-) and ⊥ (-○-) to the pseudo-chains were observed in the case of nanorods at the composition used here. Details of the magnetization curves in the directions // and ⊥ can be shown in the inset of Fig. 9b. Hence, no magnetic anisotropy effects were observed. The magnetic properties of the composites are those of the individual filler (except for the obvious "*dilution*" factor in M_s) and no additional magnetization factors are observed when forming the pseudo-chains. Thus, concerning magnetization, the structured composites with nanorods do not display anisotropy at the filler composition used in this work, and the magnetic features of the individual fillers appear conserved without changes. However, small anisotropy effects were observed in the case of nanoparticles-A when using a larger proportion in the composite (5 % w/w, Fig. 9a). In that case, small differences in M_s and M_r (but not in H_c) between curves for $\alpha = 0°$ and 90° were observed (slightly larger values for $\alpha = 0°$, that is in the direction of the pseudo-chains), suggesting a little degree of magnetic anisotropy related to the alignment of the pseudo-chains in $\alpha = 0°$, as it was published in our previous work (Antonel et al. 2011). The non-detection of anisotropic magnetic effects in composites with nanorods seems to be related to the low filler proportions used here.

Compression stress–strain curves were recorded for the directions // and ⊥ to the pseudo-chains. In all cases the composites display elastic behavior with low hysteresis (results not shown), a behavior that is similar to that observed in our previous works for related systems in PDMS at low filler proportions (less than 5 % w/w). Figure 10 illustrates L/L_i versus P curves that are calculated from the stress–strain

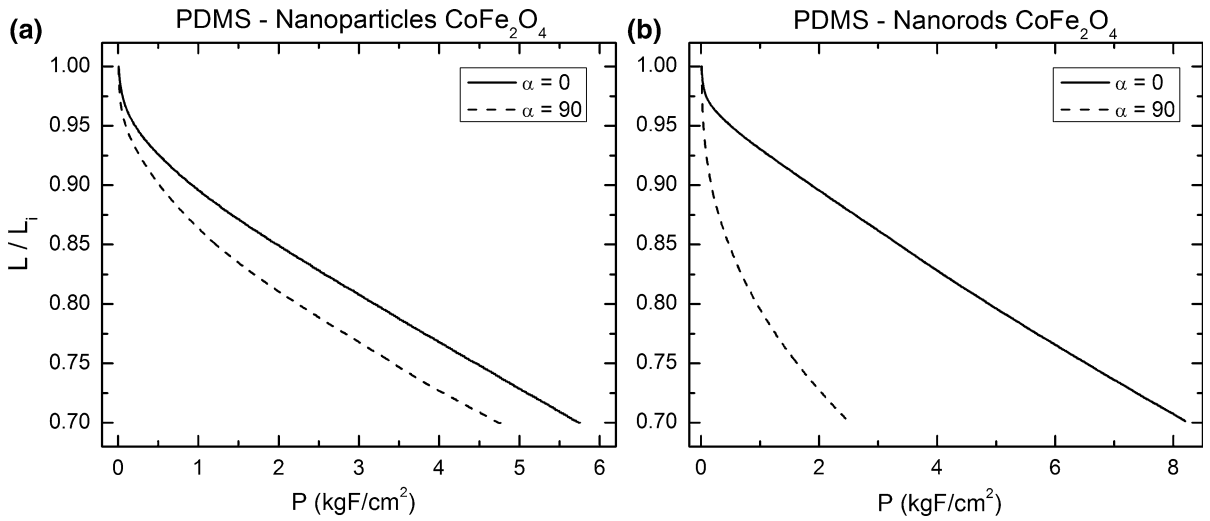

Fig. 10 Relative thickness (L/L_i) versus applied stress (P) in PDMS–$CoFe_2O_4$-structured composites using **a** nanoparticles (5 % w/w) and **b** nanorods (1 % w/w) as fillers. Curves with $\alpha = 0°$ and $\alpha = 90°$ correspond to compressions parallel and perpendicular to the pseudo-chains, respectively

analysis, where P stands for the applied stress, L refers generically to the thickness of the sample, and L_i the thickness in the absence of stress. For stresses larger than 0.3 KgF/cm^2, the curves were well fitted by single exponential decays for compressions in both directions (// and $\perp$ to the pseudo-chains), obtaining different decay constants, referred as $b_{\parallel}$ and $b_{\perp}$ (expressed in KgF/cm^2). The lower decay constant was obtained in the case of composites with nanoparticles-A in the $\perp$ direction (4–8 kgF/cm^2, considering different replicates). Although association of the decay constant obtained from compression stress–strain curves with the Youngs modulus must be taken with care (stress–strain tensile tests must be considered), the mentioned range covers with good agreement many of the Young's modulus values of PDMS reported previously (see Cheng et al. 2010; Inglis 2010; Tong et al. 2008) considering that they are influenced by the exact proportion of base polymer and cross-linker agent, the proportion of vinyl and methyl terminations in the oligomers, curing temperatures, etc.

In all considered cases, including replicates, values of $b_{\parallel}$ larger than $b_{\perp}$ were recovered ($b_{\parallel}/b_{\perp} > 1$), indicating that it requires larger stresses to be applied in the direction // than $\perp$ to obtain the same strain. This anisotropic elastic behavior can be directly appreciated, for the case on nanorods as fillers, in Fig. 10b. The percentage difference of $b_{\parallel}$ and $b_{\perp}$ is an indication of the elastic anisotropy: in the case of using nanoparticles-A, the difference between $b_{\parallel}$ and $b_{\perp}$ is about 190 % ($b_{\parallel}/b_{\perp} \approx 3$) but about 1200 % ($b_{\parallel}/b_{\perp} \approx 13$) when nanorods are used as fillers. The variation in the generated elastic anisotropy by magnetic alignment of fillers is close to one order of magnitude when using the nanorods described in this work. The elastic anisotropy is also about one order of magnitude larger than in the case of using Ni nanochains (Landa et al. 2013). This is one of the main results of the present work: very much large elastic anisotropy appears in the structured composites when using magnetic $CoFe_2O_4$ nanorods instead $CoFe_2O_4$ nanoparticles as fillers. Moreover, this large anisotropic effect is obtained with lower concentration of nanorods than nanoparticles.

Conclusions

The synthetic procedure provided the possibility to obtain $CoFe_2O_4$ nanotubes, nanorods, and nanowires with excellent purity and crystalline degree. The picture emerging from XRD, SEM, and SAXS experiments is that nanotubes and nanorods are formed by

agglomerated clusters of the inorganic material with remarkable magnetic properties. In particular, nanotubes and nanorods present coercive fields that are three times larger than those of $CoFe_2O_4$ nanoparticles of similar crystallite size. This is a characteristic of high relevance for many applications in magnetic memory devices, allowing tuning the magnetic parameters by changing the morphology of the nanomaterial. These magnetic features are conserved when the material is used as filler in the elastomer, even when—by application of a magnetic field during curing—fillers are agglomerated forming aligned pseudo-chains in the matrix. That is, the formation of aligned pseudo-chains does not disturb the magnetic properties of the fillers. The invariability is such that no magnetic anisotropy was detected at least at the relatively low loading concentrations used here.

On the other hand, the formation of aligned pseudo-chains generates a very high elastic anisotropy, not only when comparing with $CoFe_2O_4$ nanoparticles as fillers, but also much larger than the observed when using Ni nanochains of higher aspect ratio. This effect is related not only to the intrinsic rigid and anisotropic structure of the individual nanorods but also to the fact that they appear aligned in the direction H_{curing} when forming the pseudo-chains. That is, the composite is not only formed by aligned pseudo-chains, but each pseudo-chain is formed by bunches of aligned nanorods. The confluence of those factors: use of morphologically anisotropic individual fillers, formation of aligned bunches of fillers, and formation of aligned pseudo-chains with those bunches, renders in the highly anisotropic elasticity of the final composite.

Acknowledgments PSA, GJ, and RMN are research members of the National Council of Research and Technology (CONICET, Argentina). Financial support was received from the Ministry of Sciences (MINCYT-FONCYT PICT 2011-0377) and University of Buenos Aires (UBACyT 2012-2015 20020110100098). CLPO is supported by FAPESP, CNPq, and INCTFcx, Brazil. The authors thank to the Center of Advanced Microscopy (CMA) at the School of Sciences (UBA) for obtaining the presented images and pictures. AGL thanks to A. Petragalli for obtaining diffraction data and Mg. Mariana Lali (CNEA) for helping with SAED indexs and Ministry of Sciences for the financial support (ANPCyT PICT 2012-1506).

Conflict of interest The authors declare that they have no conflict of interest.

Appendix

Fractal Cluster Model

In this model, the cluster is assumed to consist of subunits that are aggregated into a ramified structure. For the subunits, we use the form factor for sphere with radius R, given by Eq. (1).

$$P(q) = F(q)^2 = \left[3\frac{\sin(qR) - qR\cos(qR)}{(qR)^3}\right]^2. \tag{1}$$

The structure factor for fractal arrangement of the subunits is described by Teixeira (1998):

$$\begin{aligned} S(q) &= 1 + \frac{D}{R^D}\int_0^\infty r^{D-1}\exp(-r/\xi)\frac{\sin(qr)}{qr}\mathrm{d}r \\ &= 1 + \frac{1}{(qR)^D}\frac{D\Gamma(D-1)}{\left[1+1/\left(q^2\xi^2\right)\right]^{(D-1)/2}} \\ &\quad \times \sin\left[(D-1)\tan^{-1}(Q\xi)\right], \end{aligned} \tag{2}$$

where D is the fractal dimension, R is the dimension of the subunits building the fractal, and ξ gives the size of the fractal. The radius of gyration of the fractal can be calculated as

$$R_g = \sqrt{D(D+1)\xi^2/2}. \tag{3}$$

For some samples, we observed a decrease in intensity at low q. This can be interpreted as being due to cluster–cluster interference. The simplest way to describe it is by the use of a simple hard-sphere structure factor $S_{\text{HS}}(q)$, as this function depends only on two (effective) parameters: R_{HS}, which is an effective hard-sphere radius, and η_{HS}, which is an effective volume fraction of hard spheres. The hard-sphere structure factor $S_{\text{HS}}(q)$ is given by Kinning and Thomas (1984):

$$S_{\mathrm{HS}}(q) = \frac{1}{1 + 24\eta G(2R_{\mathrm{HS}}q)/(2R_{\mathrm{HS}}q)}, \tag{4}$$

where

$$G(A) = \frac{a(\sin A - A\cos A)}{A^2} + \frac{\beta(2A\sin A + (2 - A^2)\cos A - 2)}{A^3} + \frac{\gamma\left[-A^4 cpsA + 4\left\{(3A^2 - 6)\cos A + (A^3 - 6A)\sin A + 6\right\}\right]}{A^5}, \tag{5}$$

and

$$\alpha = \frac{(1 + 2\eta)^2}{(1 - \eta)^4}, \quad \beta = \frac{-6\eta(1 + \eta/2)^2}{(1 - \eta)^4}, \quad \gamma = \frac{\eta\alpha}{2}. \tag{6}$$

With this, the intensity is then given as

$$I(q) = P(q)S(q)S_{\mathrm{HS}}(q). \tag{7}$$

There are interesting features for this expression. If the fractal domains, defined by overall size ξ, are smaller than the size of the overall hard-sphere interactions $\langle R_{\mathrm{HS}}\rangle$, at low angles, we might have a decrease of the scattering intensity, which indicates that the fractal domains interacts as hard spheres among each other. This concept is important to understand the results that are discussed in the text.

References

Albrecht O, Zierold R, Allende S, Escrig J, Patzig C, Rauschenbach B, Nielsch K, Görlitz D (2011) Experimental evidence for an angular dependent transition of magnetization reversal modes in magnetic nanotubes. J Appl Phys 109:093910–093914

Antonel PS, Jorge GA, Perez O, Butera A, Leyva AG, Negri RM (2011) Magnetic and elastic properties of $CoFe_2O_4$-PDMS magnetically oriented elastomer nanocomposites. J App Phys 110:43920–43928

Antonel PS, Negri RM, Leyva AG, Jorge GA (2012) Anisotropy and relaxation processes of uniaxially oriented $CoFe_2O_4$ nanoparticles dispersed in PDMS. Physica B 407: 3165–3167

Bance S, Fischbacher J, Schrefl T, Zins I, Rieger G, Cassignol C (2014) Micromagnetics of shape anisotropy based permanent magnets. J Mag Mag Mat 363:121–124

Bechelany M, Amin A, Brioude A, Cornu D, Miele P (2012) ZnO nanotubes by template-assisted sol–gel route. J Nanopart Res 14:980–986

Bellino MG, Sacanell JG, Lamas DG, Leyva DG, Walsöe NE (2007) High-performance solid-oxide fuel cell cathodes based on cobaltite nanotubes. J Am Chem Soc 129:3066–3067

Bica I, Liu YD, Choi HJ (2012) Magnetic field intensity effect on plane electric capacitor characteristics and viscoelasticity of magnetorheological elastomer. Colloid Polym Sci 290:1115–1122

Butera A, Alvarez N, Jorge GA, Ruiz MM, Mietta JL, Negri RM (2012) Microwave response of anisotropic magnetorheological elastomers: model and experiments. Phys Rev B 86:144424–144428

Cernea M, Trupina L, Vasile BS, Bartha C, Radu R, Chirila C, Teodorescu A (2014) $BiFeO_3$ doped-BNT-BT0.08 piezoelectric and magnetic nanowires, derived from sol–gel precursor. J Nanopart Res 16:2231–2238

Chen L, Jerrams S (2011) A rheological model of the dynamic behaviour of magnetorheological elastomers. J Appl Phys 110:013513–013516

Chen AP, Guslienko KY, Gonzalez J (2010) Magnetization configurations and reversal of thin magnetic nanotubes with uniaxial anisotropy. J Appl Phys 108:083920–083927

Cheng Q, Sun Z, Meininger GA, Almasri M (2010) Mechanical study of micromachined polydimethylsiloxane elastic microposts. Rev Sci Instrum 81:106104–106106

Danas K, Kankanala SV, Triantafyllidis N (2012) Experiments and modeling of iron-particle-filled magnetorheological elastomers. J Mech Phys Solids 60:120–138

Escrig J, Lavín R, Palma JL, Denardin JC, Altbir D, Cortés A, Gómez H (2008) Geometry dependence of coercivity in Ni nanowire arrays. Nanotechnology 19:075713

Forster H, Bertram N, Wang X, Dittrich R, Schrefl T (2003) Energy barrier and effective thermal reversal volume in columnar grains. J Mag Mag Mat 267:69–79

Fuentes RO, Muñoz FF, Acuña LM, Leyva AG, Baker RT (2008a) Preparation and characterization of nanostructured gadolinia-doped ceria tubes. J Mater Chem 18:5689–5695

Fuentes RO, Acuña LM, Zimicz MG, Lamas DG, Sacanell JG, Leyva AG, Baker RT (2008b) Chem Mater 20:7356–7363

Gajbhiye NS, Srivastava S, Kurian S, Behta BR, Singh VN (2010) Magnetic Field Assisted Hydrothermal Synthesis of CoFe2O4 Nanowires. J Phys Conf Ser 200: 072093

Grobert N, Hsu WK, Zhu YQ, Hare JP, Kroto HW, Walton DRM, Terrones M, Terrones H, Redlich Ph, Rühle M, Escudero R, Morales F (1999) Enhanced magnetic coercivities in Fe nanowires. Appl Phys Lett 75:3363–3364

Holz A, Scherer C (1994) Topological theory of magnetism in nanostructured ferromagnets. Phys Rev B 50:6209–6232

Høyer H, Knaapila M, Kjelstrup-Hansen J, Helgesen G (2012) Microelectromechanical strain and pressure sensors based on electric field aligned carbon cone and carbon black particles in a silicone elastomer matrix. J Appl Phys 112:094324–094328

Hussain ST, Siddiq ASM, Ali S (2011) Iron-doped titanium dioxide nanotubes: a study of electrical, optical, and magnetic properties. J Nanopart Res 13:6517–6525

Inglis DW (2010) A method for reducing pressure-induced deformation in silicone microfluidics. Biomicrofluidics 4:026504–026511

Jung JS, Lim JH, Choi KH, Oh SL, Kim YR, Lee SH, Smith DA, Stokes KL, Malkinski L, O'Connor CJ (2005) $CoFe_2O_4$ nanostructures with high coercivity. J Appl Phys 97:10F306–10F309

Kinning DJ, Thomas EL (1984) Hard-sphere interactions between spherical domains in diblock copolymers. Macromol 17:1712–1718

Ko TY, Tsai MH, Lee CS, Sun KW (2012) Electron transport mechanisms in individual cobalt-doped ZnO nanorods. J Nanopart Res 14:1253–1265

Kohli S, McCurdy PR, Johnson DC, Das J, Prieto AL, Rithner CD, Fisher ER (2010) Template-assisted chemical vapor deposited spinel ferrite nanotubes. J Phys Chem C 114:19557–19561

Landa RA, Antonel PS, Ruiz MM, Perez OE, Butera A, Jorge GA, Oliveira CLP, Negri RM (2013) Magnetic and elastic anisotropy in magnetorheological elastomers using nickel-based nanoparticles and nanochains. J App Phys 114: 213912–213922

Landeros P, Núñez AS (2010) Domain wall motion on magnetic Nanotubes. J Appl Phys 108:033917–033926

Leslie-Pelecky DL, Rieke RD (1996) Magnetic properties of nanostructured. Mater Chem Mater 8:1770–1783

Levy P, Leyva AG, Troiani H, Sanchez RD (2003) Nanotubes of rare earth manganese oxide. Appl Phys Lett 83:5247–5249

Leyva AG, Stoliar P, Rosenbusch M, Levy P, Curiale J, Troiani H, Sanchez RD (2004) Synthesis route for obtaining manganese oxide based nanostructures. Phys B 354: 158–160

Leyva AG, Curiale J, Troiani H, Rosenbusch M, Levy P, Sánchez RD (2006) Nanoparticles of $La_{1-x}Sr_xMnO_3$ ($x = 0.33, 0.20$) assembled into hollow nanostructures for solid oxide fuel cells. disclosing materials at the nanoscale. Adv Sci Technol 51:54–59

Lorenzo D, Fragouli D, Bertoni G, Innocenti C, Anyfantis GC, Cozzoli PD, Cingolani R (2012) Formation and magnetic manipulation of periodically aligned microchains in thin plastic membranes. J Appl Phys 112:083927–083934

Macias JD, Ordonez-Miranda J, Alvarado-Gil JJ (2012) Resonance frequencies and Young's modulus determination of magnetorheological elastomers using the photoacoustic technique. J Appl Phys 112:124910–124917

Mietta JL, Ruiz MM, Antonel PS, Perez OE, Butera A, Jorge GA, Negri RM (2012) Anisotropic magnetoresistance and piezoresistivity in structured Fe_3O_4–silver particles in PDMS elastomers at room temperature. Langmuir 28:6985–6996

Mietta JL, Jorge GA, Perez OE, Maeder T, Negri RM (2013) Superparamagnetic anisotropic elastomer connectors exhibiting reversible magneto-piezoresistivity. Sens Actuat A 192:34–41

Mietta JL, Jorge GE, Negri RM (2014) A flexible strain gauge exhibiting reversible piezoresistivity based on an anisotropic magnetorheological polymer. Smart Mater Struct 23:85026–85038

Mordina B, Tiwari RJ, Setua DK, Sharma A (2014) Magnetorheology of polydimethylsiloxane elastomer/$FeCo_3$ nanocomposite. J Phys Chem C 118:25684–25703

Negri RM, Rodriguez SD, Bernik DL, Molina FV, Pilosof A, Pérez OE (2010) A model for the dependence of the electrical conductance with the applied stress in insulating-conducting composites. J Appl Phys 107:113703–113714

Pereira A, Gallardo C, Espejo AP, Briones J, Vivas LG, Vázquez M, Denardin JC, Escrig J (2013) Tailoring the magnetic properties of ordered 50-nm diameter CoNi nanowire arrays. J Nanopart Res 15:2041–2048

Ruiz MM, Antonel PS, Perez OE, Negri RM, Jorge GE (2012) Structural and magnetic properties of $Fe_{2-x}CoSm_xO_4$-nanoparticles and $Fe_{2-x}CoSm_xO_4$–PDMS magnetoelastomers as a function of Sm content. J Mag Mag Mater 327:11–19

Ruiz MM, Marchi MC, Perez OE, Jorge GE, Mirta F, Norma D'Accorso, Martín Negri R (2015) Structured elastomeric submillimeter films displaying magneto and piezo resistivity. J Pol Sci B. doi:10.1002/polb.23672

Semeriyanov F, Chervanyov AI, Jurk R, Subramaniam K, Konig S, Roscher M, Das A, Stockelhuber KW, Heinrich GJ (2013) Non-monotonic dependence of the conductivity of carbon nanotube-filled elastomers subjected to uniaxial compression/decompression. J Appl Phys 113:103706–103712

Shahrivar K, de Vicente J (2013) Where physics meets chemistry meets biology for fundamental soft matter *research*. Soft Matter 9:11451–11456

Teixeira J (1998) Small-angle scattering by fractal systems. J Appl Crystallogr 21:781–785

Thang PD, Rijnders G, Blank DHA (2007) Stress-induced magnetic anisotropy of $CoFe_2O_4$ thin films using pulsed laser deposition. J Mag Mag Mater 310:2621–2623

Tong J, Simmons CA, Yu SJ (2008) Precision patterning of PDMS membranes and applications. Micromech Microeng 18:037004–037007

Tsai MC, Lin GT, Chiu HT, Lee CY (2008) Synthesis of zirconium dioxide nanotubes, nanowires, and nanocables by concentration dependent solution deposition. J Nanopart Res 10:863–869

Usov NA, Serebryakova ON (2014) The peculiarities of magnetization reversal process in magnetic nanotube with helical anisotropy. J Appl Phys 116:133902–133909